2016

Contact resonances of U-shaped atomic force microscope probes

E. Rezaei
University of Nebraska-Lincoln

Joseph A. Turner
University of Nebraska-Lincoln, jaturner@unl.edu

Contact resonances of U-shaped atomic force microscope probes

E. Rezaei and J. A. Turner[a)]
Mechanical and Materials Engineering, University of Nebraska-Lincoln, W342 Nebraska Hall, Lincoln, Nebraska 68588, USA

(Received 6 October 2015; accepted 6 January 2016; published online 20 January 2016)

Recent approaches used to characterize the elastic or viscoelastic properties of materials with nanoscale resolution have focused on the contact resonances of atomic force microscope (CR-AFM) probes. The experiments for these CR-AFM methods involve measurement of several contact resonances from which the resonant frequency and peak width are found. The contact resonance values are then compared with the noncontact values in order for the sample properties to be evaluated. The data analysis requires vibration models associated with the probe during contact in order for the beam response to be deconvolved from the measured spectra. To date, the majority of CR-AFM research has used rectangular probes that have a relatively simple vibration response. Recently, U-shaped AFM probes have created much interest because they allow local sample heating. However, the vibration response of these probes is much more complex such that CR-AFM is still in its infancy. In this article, a simplified analytical model of U-shaped probes is evaluated for contact resonance applications relative to a more complex finite element (FE) computational model. The tip-sample contact is modeled using three orthogonal Kelvin-Voigt elements such that the resonant frequency and peak width of each mode are functions of the contact conditions. For the purely elastic case, the frequency results of the simple model are within 8% of the FE model for the lowest six modes over a wide range of contact stiffness values. Results for the viscoelastic contact problem for which the quality factor of the lowest six modes is compared show agreement to within 13%. These results suggest that this simple model can be used effectively to evaluate CR-AFM experimental results during AFM scanning such that quantitative mapping of viscoelastic properties may be possible using U-shaped probes. © *2016 AIP Publishing LLC*.
[http://dx.doi.org/10.1063/1.4940049]

I. INTRODUCTION

The development of new materials often results in heterogeneous composition that spans multiple length scales. In order for new material designs to be fully understood, measurements that can quantify behavior at appropriate scales, often down to the nanoscale, are required. The contact resonance atomic force microscope (CR-AFM) technique is a promising materials characterization approach, which can quantify the elastic[1–9] as well as viscoelastic[10–16] properties of materials with spatial resolution on the order of tens of nanometers. CR-AFM uses the vibration spectra of an AFM probe during vibrations for both the noncontact case, and when the tip is in contact with a sample. Rabe *et al.*[17] first presented this approach and included an analytical solution for the dynamic behavior of the AFM probe. More recently, Yuya *et al.*[10,18] developed a method to find the viscoelastic properties of a sample from experiment by following a similar approach. CR-AFM is becoming well accepted for analyzing the properties of a wide variety of materials such as polymers,[11–14,16,18,23] biological materials,[16,25,26] composite materials,[27] dielectric materials,[28] metallic glass,[29] and metals.[6,8,9] It has shown great promise for many interesting problems especially those involving the interfaces of a multi-phase material. These are some examples that illustrate the demand for nanoscale property measurements. The basis of CR-AFM is that each resonance shifts to a higher frequency for the contact case compared with the noncontact case, which provides the necessary data to find the sample stiffness.[17,19,20] Likewise, the change in the width of the resonances can be used to find material damping.[16,18] For both types of samples, the inversion algorithm to find the properties involves a deconvolution of the probe vibration response. Thus, the creation of quantitative images of properties from CR-AFM spectra during scanning requires simple analytical solutions of the probe vibrations in order for the inversion to be made during the experiment rather than as a post-processing step.

Recently developed U-shaped AFM probes allow a current to be passed through them to heat the tip which offers new possibilities for AFM measurements at different temperatures. Thermomechanical measurements of polymers are critical for a clear picture of their behavior. In addition, a U-shaped probe can also carry the required oscillating current which can induce the Lorentz force for interaction with a magnetic field. Lorentz force actuation allows contact resonances to be measured cleanly without the parasitic noise that is sometimes common for conventional piezoelectric excitation.[21–23] Such measurements using U-shaped probes were recently compared with a computational finite element (FE) analysis of the U-shaped probe response.[24] That work was focused on contact stiffness such that the model did not include damping. Although illustrative, such FE models are limited in many instances, because

[a)]Electronic mail: jaturner@unl.edu

manufacturing variations among individual AFM probes are still quite large such that the iterative FE modeling necessary to match experiments is not practical. The use of U-shaped probes for CR-AFM is very new, and the complex vibrations of such probes can be difficult to interpret. Thus, simple analytical models are needed to exploit the many advantages of their design.[24,30,31]

In this article, an analytical model for the vibrations of U-shaped AFM probe in contact with a viscoelastic sample is presented. The model is an extension of previous work that considered only the free (noncontact) vibrations.[32] This three-beam model (TBM) is based on the response of three connected beams which can both bend and twist. Two of the beams are parallel and define the legs of the U-shaped probe, and the third is the cross beam that is perpendicular to both legs. A comparison of the TBM with the finite element method (FEM) for the noncontact case showed that the TBM works well.[32] Here, that work is extended to the case of tip-sample contact that is modeled with three orthogonal Kelvin-Voigt viscoelastic elements. The normalized frequency and quality factor of several modes for a wide range of contact stiffness and damping are obtained from the TBM and compared with FEM. The results suggest that this simplified model is appropriate for fast analysis of CR-AFM spectra for U-shaped probes.

II. CONTACT CASE OF THE TBM

The analysis is based on the dynamics of a typical U-shaped probe in contact with a viscoelastic sample. For that goal, we consider the geometry of a commercial thermal cantilever, AN2-300, from Anasys Instruments.[33] For this type of probe, two parallel "legs" of the same length are connected with a cross beam as illustrated in Fig. 1. The two legs of the U-shaped probe are clamped at one end, and the cross beam is coupled to them at the other end. For each of the legs and cross beam, only flexural and torsional displacements are considered, and for simplicity lateral and axial displacements are neglected. This probe is modeled based on Euler-Bernoulli beam theory. It is important to note that the displacement behavior of the cross beam is an important part

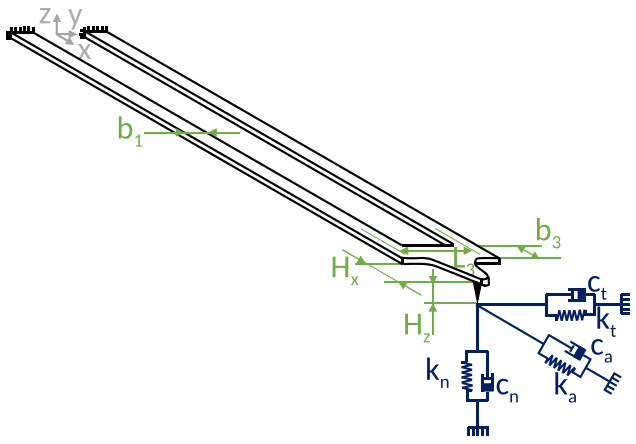

FIG. 1. Model for the U-shaped probe in contact with a viscoelastic sample. The contact is assumed to have form of three independent orthogonal Kelvin-Voigt components in the normal, axial, and transverse directions.

of the overall response. Initial models that included only a rigid cross beam did not produce the frequency behavior observed for the FEM nor experiments. Thus, the equations of motion for both flexural and torsional vibrations for each beam are given by[32]

$$EI\frac{\partial^4 w(x,t)}{\partial x^4}+\rho A\frac{\partial^2 w(x,t)}{\partial t^2}=0, \tag{1}$$

$$GK\frac{\partial^2 \phi(x,t)}{\partial x^2}-\rho J\frac{\partial^2 \phi(x,t)}{\partial t^2}=0, \tag{2}$$

where the vertical displacement w and twist angle ϕ are functions of position x (y for the cross beam) and time t. Here, I is the area moment of inertia, A is the cross-sectional area of the beam, and J is the polar area moment of inertia. The properties of the probe include E, the Young's modulus, ρ, the volumetric density, and GK, the torsional stiffness.

Geometric parameters of the U-shaped probe are depicted in Fig. 1. Here, b_1 is the leg width, b_3 is the cross beam width, L_3 is the cross beam length, and two other parameters H_x and H_z represent the axial and vertical locations of the tip-sample contact with respect to the middle of the cross beam. All of these geometrical parameters are nondimensionalized with respect to the probe length, and the tilde ($\sim$) is used to denote the dimensionless parameters. Following the geometrical parameters, time is also cast in dimensionless form, allowing a dimensionless time τ to be defined as

$$\tau=t\sqrt{\frac{(EI)_1}{(\rho A)_1 L^4}}. \tag{3}$$

Finally, the dimensionless equations of flexural and torsional motion for the three beams of the system are given by

$$\begin{aligned}
&\tilde{w}_1''''(\tilde{x},\tau)+\ddot{\tilde{w}}_1(\tilde{x},\tau)=0,\\
&\tilde{w}_2''''(\tilde{x},\tau)+S_1^4\ddot{\tilde{w}}_2(\tilde{x},\tau)=0,\\
&\tilde{w}_3''''(\tilde{y},\tau)+S_2^4\ddot{\tilde{w}}_3(\tilde{y},\tau)=0,\\
&\tilde{\phi}_1''(\tilde{x},\tau)-S_3^2\ddot{\tilde{\phi}}_1(\tilde{x},\tau)=0,\\
&\tilde{\phi}_2''(\tilde{x},\tau)-S_4^2\ddot{\tilde{\phi}}_2(\tilde{x},\tau)=0,\\
&\tilde{\phi}_3''(\tilde{y},\tau)-S_5^2\ddot{\tilde{\phi}}_3(\tilde{y},\tau)=0,
\end{aligned} \tag{4}$$

where the primes ($'$) denote partial derivatives with respect to the corresponding spatial coordinate, and the overdots ($\dot{}$) denote temporal partial derivatives. Simplified versions of the dimensionless coefficients S_i are given in Eq. (A15) of the Appendix using assumptions of a thin beam with rectangular cross section.

The TBM is a model of three beams, and for each beam the flexural vibrations (governed by a fourth-order equation) and the torsional vibrations (governed by a second-order equation) need to be considered. Thus, for solving the system, a total of eighteen boundary and continuity conditions are required.[32] The parallel beams are clamped at one end and connected to the cross beam at the other end. Therefore, application of the boundary conditions at the clamped ends reduces the complexity of the problem. The six boundary

conditions at the clamped ends, three for each leg, are given by

$$\tilde{w}_1(0,\tau)=0,\quad \frac{\partial\tilde{w}_1(0,\tau)}{\partial\tilde{x}}=0,\quad \tilde{\phi}_1(0,\tau)=0,$$
$$\tilde{w}_2(0,\tau)=0,\quad \frac{\partial\tilde{w}_2(0,\tau)}{\partial\tilde{x}}=0,\quad \tilde{\phi}_2(0,\tau)=0.$$

The other boundary and continuity conditions are defined at the joints of the legs and the cross beam. The continuity conditions of displacement and slope are given by

$$\tilde{w}_1(1,\tau)=\tilde{L}_3\tilde{w}_3\left(\frac{-1}{2},\tau\right), \tag{5}$$

$$\tilde{w}_1'(1,\tau)=\tilde{\phi}_3\left(\frac{-1}{2},\tau\right), \tag{6}$$

$$\tilde{\phi}_1(1,\tau)=\tilde{w}_3'\left(\frac{-1}{2},\tau\right), \tag{7}$$

and

$$\tilde{w}_2(1,\tau)=\tilde{L}_3\tilde{w}_3\left(\frac{1}{2},\tau\right), \tag{8}$$

$$\tilde{w}_2'(1,\tau)=\tilde{\phi}_3\left(\frac{1}{2},\tau\right), \tag{9}$$

$$\tilde{\phi}_2(1,\tau)=\tilde{w}_3'\left(\frac{1}{2},\tau\right). \tag{10}$$

Kelvin-Voigt elements are used to model the tip-sample contact as shown in Fig. 1. These elements are defined in the axial (k_a, c_a), normal (k_n, c_n), and transverse (k_t, c_t) directions. Each spring and dashpot introduces forces and moments that contribute to the overall eigenvalue problem. Thus, six more continuity conditions at the joints are used to define the continuity of force. These continuity conditions are discussed in detail in the Appendix.

The external damping and stiffness which come from the contact can be nondimensionalized with respect to the equivalent probe stiffness. The equivalent bending stiffness of the U-shaped probe can be estimated as two times the leg stiffness, or $6EI/L^3$. Dimensionless variables for contact stiffness and damping, α and β, are then defined as

$$\alpha_{n,t,a}=\frac{k_{n,t,a}}{\frac{6EI}{L^3}}\qquad \beta_{n,t,a}=c_{n,t,a}\sqrt{\frac{L^2}{36EI\,\rho A}}, \tag{11}$$

where the indices n, t, and a represent the contact directions. These dimensionless variables arise from the continuity conditions which define the load relations (see the Appendix). They subsequently appear in the characteristic equation of the system that defines the wavenumbers for the system in contact, which means that they also affect the contact resonances. The dimensionless relation between wavenumber (κ) and frequency (f) can be written as

$$\omega^2=(2\pi f)^2=\frac{\kappa^4}{L^4}\frac{EI}{\rho A}, \tag{12}$$

which implies that

$$f=\frac{\kappa^2}{2\pi L^2}\sqrt{\frac{E\tilde{h}^2}{12\rho}}, \tag{13}$$

where L is the length of the legs, and $\tilde{h}$ is the dimensionless cantilever thickness. Equation (13) is written under the assumption that the cross section of each beam is rectangular.

As discussed above, the coupled vibrational motion of a U-shaped probe, considering only flexural and torsional motion, results in a system of 18 equations with 18 unknowns.[32] Application of the clamped boundary conditions reduces the number of equations to 12, which define the eigenvalue problem for the contact case. Six of the continuity conditions are expressed in Eqs. (5)–(10) and the other six are stated in Eqs. (A4)–(A9). As discussed previously,[32] Eq. (4) can be solved by separation of variables for the flexural and torsional motion of the legs and cross beam. The resulting eigenvalue problem is defined from these continuity conditions. The determinant of the matrix of coefficients of the unknowns is the characteristic equation, from which the roots define the natural frequencies and Q-factors for all resonances. When the tip is not in contact with the sample, and assuming no damping from the surrounding fluid or within the probe material, the resulting equations are entirely real.[32] When damping in the tip-sample contact is considered, the governing equations are no longer strictly real. In this case, these equations acquire an imaginary part that comes from the damping of the sample defined by the dashpots. Due to the temporal derivative in velocity, the imaginary part appears in these equations. A schematic of the system of equations for both the noncontact and contact cases can be illustrated as

$$\left\{\underbrace{\begin{bmatrix}12\times12\end{bmatrix}}_{\text{Free (real)}}+\underbrace{\begin{bmatrix}12\times12\\ k_n,k_a,k_t\end{bmatrix}}_{\text{Contact (real)}}+\underbrace{\begin{bmatrix}12\times12\\ c_n,c_a,c_t\end{bmatrix}}_{\text{Contact (imaginary)}}\right\}\times[\,\text{eigenvector}\,]=\underline{\underline{0}}. \tag{14}$$

The solution of the eigenvalue problem given by the schematic Eq. (14) for the noncontact case shows that this type of the probe has two different kinds of flexural modes. For the first type of mode, the legs move in phase with each other such that these modes are called "symmetric." Other modes exhibit motion with the legs moving out of phase with each other such that these modes are called "asymmetric." Although the cross beam also has its own vibrational response that is coupled with the two legs, here the modes are identified based primarily on the leg motion. The symmetric modes have simpler motion that is similar to that of rectangular beams studied previously. The mode shapes for the asymmetric modes are more complicated. For instance, the first asymmetric mode results in very little vertical motion of the tip because the crossbeam behavior is dominated by rigid body deflection, as depicted in Fig. 2(b).

The wavenumbers obtained from the TBM, i.e., Eq. (14), are complex when damping is included. The quality factor of each mode is related to the corresponding complex wavenumber.[10,18] Each dimensionless complex wavenumber is defined as $\kappa_r = a_r + ib_r$, where a_r and b_r denote the real and imaginary parts of the wavenumber, respectively. The free vibration amplitude of the *rth* mode of the system is given by

$$G(i\omega) = \frac{1}{N\kappa_r^4 - \omega^2 + i\omega\bar{\chi}}, \tag{15}$$

where $N = EI/\rho A\, L^4$, and $\bar{\chi}$ is dimensionless beam damping. By assuming that the imaginary part of the wavenumber is smaller than the real part (i.e., $b_r \ll a_r$), the response for this mode can be written as[10]

$$G(i\omega) = \frac{1}{\left(Na_r^4 - \omega^2\right) + i\left(4Na_r^3 b_r\right)}. \tag{16}$$

Near the resonance, the response should be significant, which implies that the real part of the denominator must be equal to zero such that

$$Na_r^4 = \omega_n^2. \tag{17}$$

Substituting Eq. (17) into Eq. (16) and dividing by ω_n^2 gives

$$\tilde{G}(i\omega) = \frac{1}{\left(1 - \omega^2/\omega_n^2\right) + i\left(4\omega_n^2 b_r/a_r\right)/\omega_n^2}. \tag{18}$$

The frequency response equation based on the natural frequency and viscous damping factor can be stated as[34]

$$\tilde{G}(i\omega) = \frac{1}{\left(1 - \omega^2/\omega_n^2\right) + i2\zeta\omega/\omega_n}. \tag{19}$$

Evaluating Eqs. (18) and (19) at the resonant frequency, and comparing them to each other, the relation of the quality factor and wavenumber for each mode can be found as

$$Q_r = \frac{a_r}{4b_r}. \tag{20}$$

In Sec. III, the finite element formulation of the same vibration problem is discussed. Of particular emphasis is the damped problem for which the determination of quality factor is nontrivial. Then, comparisons between the two models are made for both the elastic and viscoelastic cases.

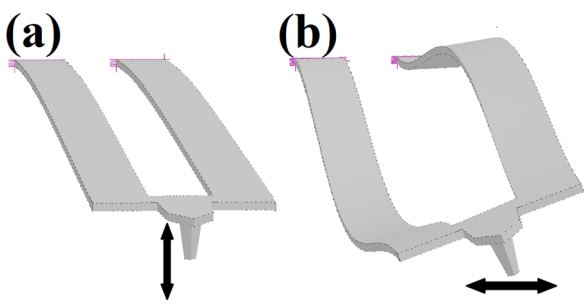

FIG. 2. Motion of the tip for different types of flexural modes: (a) when the modes are "symmetric," the tip moves primarily up and down (out-of-plane of the sample), and (b) when the modes are "asymmetric," the tip moves primarily tangent to the sample.

III. FE MODELING

The U-shaped probe is also modeled using commercial FE software (Abaqus). It is meshed using 20-node quadratic brick elements, which have nodes at their corners as well as their midside. To remove possible mesh dependency and also to be efficient in time and memory, the probe is meshed with 3000 elements in the main body. The tip and extended part of the probe are assumed to be massless and rigid (imposing much higher stiffness), and these parts also are meshed with the same type of element.

As with the analytical model, contact in the FEM is also modeled using three orthogonal Kelvin-Voigt elements. Each element connects the end point of the tip to ground, and they are defined in the normal, axial, and transverse directions. The elements of contact are defined such that each has an influence only in the assumed direction for any type of probe motion (i.e., the elements are not allow to rotate). The contact elements available in the FE software allow the contact to be defined for both the damped and undamped cases.

In the FEM, the ratio of the leg width to the length of the probe is 0.052, and this value for the cross beam width is 0.034. The dimensionless cross beam length is 0.11, and the thickness of the probe is 0.007 of the length of the probe, which is the same through the whole probe. The Young's modulus for the model is chosen as 130 GPa, Poisson's ratio as 0.22, and the density as 2329 kg/m^3. The selected properties are representative of silicon. Although single-crystal silicon is anisotropic, here the probe is considered to be isotropic for simplification. The analytical TBM also assumes material isotropy.

A. FEM modal analysis

In CR-AFM, the properties of the resonant peaks are key factors that need to be determined, and the two most important properties are the resonant frequency and its width or quality factor. Thus, these parameters will be used for comparison between the FEM and TBM. The output of the FEM software can be obtained by solving the problem in two steps. The first step of the FEM gives an output of the frequencies alone, and after the second step the software provides both the real and imaginary parts of the eigenvalues. The complex eigenvalues resulting from the FE software must then be interpreted in order to identify the resonant frequencies and quality factors for all modes. The meshed equations of motion of the resulting n-degree-of-freedom system can be put in matrix form assuming arbitrary viscous damping as

$$\underline{\underline{M}}\ddot{\underline{q}} + \underline{\underline{C}}\dot{\underline{q}} + \underline{\underline{K}}\,\underline{q} = 0, \tag{21}$$

which governs the displacement vector $\underline{q}$ with the overdots denoting temporal derivatives. Here, $\underline{\underline{M}}$ is the system mass matrix, $\underline{\underline{C}}$ represents the damping matrix, and $\underline{\underline{K}}$ denotes the stiffness matrix of the system. The solution for this set of *n*

equations requires the problem first to be expressed in the *state space* form.[34,35] In this case, two obvious identities are introduced by rearrangement of Eq. (21) as

$$\dot{\underline{q}}(t) = \dot{\underline{q}}(t), \ddot{\underline{q}}(t) = -\underline{\underline{M}}^{-1}\underline{\underline{C}}\dot{\underline{q}}(t) - \underline{\underline{M}}^{-1}\underline{\underline{K}}\,\underline{q}(t). \tag{22}$$

Then, the *state vector* $\underline{x}(t)$ is defined by

$$\underline{x}(t) = \begin{bmatrix} \underline{q}(t) \\ \dot{\underline{q}}(t) \end{bmatrix}. \tag{23}$$

Equation (22) can then be rewritten in state form as

$$\dot{\underline{x}}(t) = \underline{\underline{A}}\,\underline{x}(t), \tag{24}$$

where the matrix of coefficients, $\underline{\underline{A}}$, is given by

$$\underline{\underline{A}} = \begin{bmatrix} \underline{\underline{0}} & \underline{\underline{I}} \\ -\underline{\underline{M}}^{-1}\underline{\underline{K}} & -\underline{\underline{M}}^{-1}\underline{\underline{C}} \end{bmatrix}. \tag{25}$$

The solution of the *state equation*, Eq. (24), can be obtained by means of a modal analysis in the state space, and its solution is assumed to have exponential form

$$\underline{x}(t) = \underline{X}e^{\lambda t}, \tag{26}$$

where $\underline{X}$ is a constant vector (eigenvector), and λ is a complex scalar constant (the eigenvalue). Here, the eigenvalue can be a complex number, so that the solution can be rewritten as

$$\underline{x}(t) = \underline{X}e^{\lambda_R t}e^{i\lambda_I t} \qquad \lambda_R \leq 0, \tag{27}$$

where λ_R and λ_I define the real and imaginary parts of the eigenvalue, respectively, with both values assumed to be strictly real. The analogous response of a damped single degree of freedom system is given by[34]

$$x(t) = Xe^{-\zeta\omega_n t}e^{i\omega_d t}, \tag{28}$$

where the damped natural frequency, ω_d, is related to damping factor, ζ, and undamped natural frequency, ω_n, by

$$\omega_d = \omega_n\sqrt{1-\zeta^2}. \tag{29}$$

Equations (27) and (28) imply a relation among the eigenvalue, the natural frequency, and the damping factor such that

$$\omega_n = f(\lambda_R, \lambda_I), \tag{30}$$

$$\zeta = g(\lambda_R, \lambda_I). \tag{31}$$

Comparison of the solution stated in Eq. (27) with the one given in Eq. (28) shows that the natural frequency and damping factor can be found in terms of the real and imaginary parts of the eigenvalues. They are thus defined as

$$\omega_n^2 = \lambda_R^2 + \lambda_I^2, \tag{32}$$

$$\zeta = -\frac{\lambda_R}{\omega_n}. \tag{33}$$

Equations (32) and (33) now give the relation connecting the complex eigenvalues obtained from the FEM solution with the physical terms, which can be acquired from the TBM frequency spectra peak analysis.

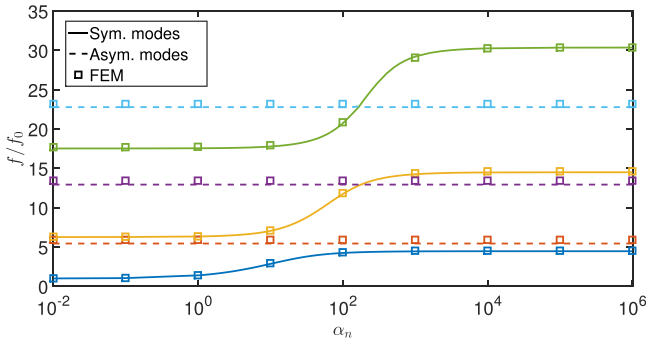

FIG. 3. Variation of the natural frequencies of the U-shaped probe to the normal contact stiffness alone (all damping is zero and $\alpha_a = \alpha_t = 0$). The solid lines show the normalized frequency variation of the symmetric modes; dashed lines illustrate the change of the normalized frequency of asymmetric modes; markers denote the results from FEM for several values.

The quality factor of each mode is then obtained from the viscous damping factor.[34] Substitution of Eq. (32) into Eq. (33) gives the relation of viscous damping factor to the real and imaginary parts of eigenvalues explicitly. Finally, the quality factor can be expressed in terms of the FEM eigenvalues as

$$Q \cong \frac{1}{2\zeta} = -\frac{\sqrt{1+\left(\frac{\lambda_I}{\lambda_R}\right)^2}}{2}. \tag{34}$$

IV. RESULTS

The comparison between the TBM and FEM is comprised of two parts. First, the results for the undamped contact case are presented, and then the results that include damping in the contact are shown. For both aspects, we first examine individual components of the contact (i.e., a single Kelvin-Voigt element) and then examine the combined effect for which specific relations are assumed between the axial and transverse elements in terms of the normal. It is important to note, however, that all parameters of the tip-sample contact are independent in reality and will need to be evaluated as such for comparison with experiments.

A. Undamped contact vibrations

Figures 3–5 depict the results for undamped vibration frequencies as a function of dimensionless contact stiffness (all damping is zero). The values for the resonant frequency are shown in normalized form, relative to the first noncontact frequency (i.e., the fundamental frequency f_0). Solid and dashed lines in the figures represent the resonant frequencies from the TBM for symmetric and asymmetric modes, respectively. The FEM results are shown at several values using square markers. The TBM calculations are much faster than FEM so that smooth curves can be generated over a wide range of contact stiffness. The selected FEM values were chosen to span the same range. The lowest value of the contact stiffness is only 1% of the probe equivalent stiffness such that the lowest value is representative of the noncontact case for these six modes. On the other hand, the upper end of

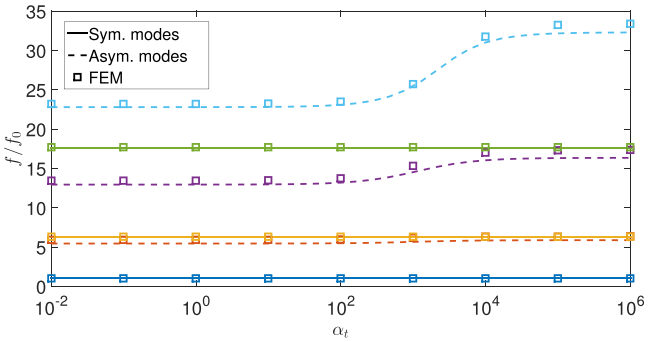

FIG. 4. Variation of the natural frequencies of the U-shaped probe to the transverse contact stiffness α_t alone (all damping is zero and $\alpha_a = \alpha_n = 0$). The solid lines show normalized frequency variation of the symmetric modes; dashed lines illustrate the change of the normalized frequency of asymmetric modes; markers denote the results from FEM for several values.

contact stiffness (one million times the probe equivalent stiffness) represents the case for which the tip-sample contact may be considered to be "pinned" for all six modes. Although such a high contact stiffness is perhaps unphysical, it allows the upper plateau region to be clearly examined.

In general, the frequency change of each mode shows sensitivity primarily to the stiffness component that restricts its motion. Thus, a vertical restriction to a mode that does not have any motion in this direction does not show any frequency shift (e.g., the asymmetric modes in Fig. 3 are unchanged with respect to normal contact stiffness). By contrast, modes with large vertical modal displacements at the tip will show the most significant changes with normal contact stiffness. Thus, the mode shape also plays an important role in the results presented here, as illustrated in Fig. 2. The results in Fig. 3 show the change in frequency relative to the normal stiffness only ($\alpha_a = \alpha_t = 0$). We see that the first symmetric frequency begins at unity and increases up to about 5 times the fundamental. The normalized frequency of the second symmetric mode increases about three times from 5 to slightly less than 15. The normalized frequency of the third symmetric mode also increases about 75% from about 17 to 30 due to the stiffening of the contact in the normal direction. For these results, the symmetric modes behave similarly to rectangular AFM probes studied previously. As expected, the asymmetric modes show no change to normal contact

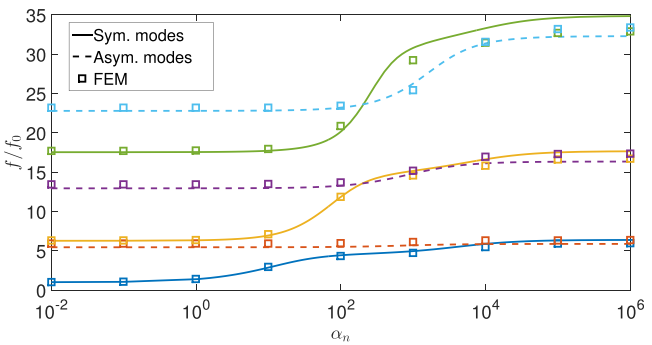

FIG. 5. Variation of the natural frequencies of the U-shaped probe with respect to α_n for the case with $\alpha_a = \alpha_t = 0.85\alpha_n$ (all damping is zero). The solid lines show normalized frequency variation of the symmetric modes; dashed lines illustrate the change of the normalized frequency of asymmetric modes; markers denote the results from FEM for several values.

stiffness variation. For this example, the TBM predicts the frequency response very well relative to the FEM. In particular, there are some residual differences between the TBM and FEM solutions from the noncontact solution, which stay unchanged for the asymmetric modes. These are about 8%, 3.75%, and 1.75% for first, second, and third asymmetric modes, respectively. The difference of TBM versus FEM for the symmetric modes varies with contact stiffness. The first symmetric mode of the TBM has only a half a percent error compared with the FEM for the noncontact case, which increases to 1.4% for high contact stiffness. The second symmetric mode has an error of a half percent too, and it stays less than 1% even for high values of normal contact stiffness. Unlike the second symmetric mode, the normalized frequency of the third symmetric mode has a 1% error for the noncontact case which decreases nearly to zero when the stiffness takes a high value. By examining the changes with respect to a single tip-sample contact component, the ordering of the modes can be easily observed. For example, although the normalized frequency of the first symmetric mode is more than 300% greater than its noncontact frequency, it still does not reach the value of the first asymmetric mode. The order of the second and the third modes changes when the dimensionless normal contact stiffness is between 100 and 200. This point is especially important when experimental results are considered.

In contrast to the normal contact stiffness, the transverse contact stiffness influences only the asymmetric flexural modes, as depicted in Fig. 4. For the case considered here, the effect on the asymmetric modes is not as strong as that observed for the symmetric modes in Fig. 3. We also observe that the order of the modes is not changed by the transverse stiffness alone for the large range of values considered here. The residual error of the free TBM to the free FEM for the first asymmetric mode is about 8% and shows a slight decrease to 7.5% for very high values of α_t. The second asymmetric mode has an error of 3.75% for the free case, and it increases to 5.72% when the contact stiffness reaches its highest value. The third asymmetric flexural mode also has a similar trend as the second one. Its error relative to the FEM for the free case is 1.7%, and it increases to 3.3% for large α_t. Nearly, all of the asymmetric modes start to increase when the dimensionless transverse contact stiffness is 10, but the rate of the increase varies with mode until they reach the pinned condition.

Finally, Figure 5 shows a more realistic tip-sample contact to illustrate the complexity of this vibration problem. In this case, the in-plane stiffnesses, transverse and axial, as well as out-of-plane stiffness, normal, are all included with $\alpha_a = \alpha_t = 0.85\alpha_n$ (again without damping). Due to the inclusion of all contact stiffnesses, all modes show changes in their resonant frequency as expected. As shown in Fig. 5, the symmetric modes show an influence that occurs in two steps with increasing contact stiffness. The earlier more significant rise happens for lower values of the stiffness and it correlates with the response observed for the normal contact stiffness alone, while the second change results from the axial contact stiffness. As mentioned previously, the asymmetric modes are affected only by the transverse contact stiffness variation.

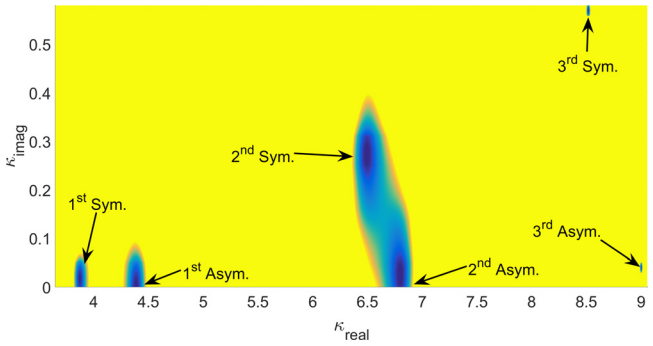

FIG. 6. The complex roots of the characteristic equation are governed by the determinant of the matrix shown in Eq. (14). The local minima for this determinant define the real and imaginary parts of the complex wavenumber for each mode. The results shown are for the case with $\alpha_n = 100$, $\beta_n = 1$ with all other contact elements zero.

The TBM compares well with the FEM for a wide range of stiffness, and the trends of both models are very similar. The difference in the frequencies of the modes of the TBM compared with the FEM for the pinned case is less than 8% for all modes. These results also show how complicated the vibration response of these probes can be. The third and fourth modes are of particular interest because they clearly have a very close spacing for a wide range of contact stiffness suggesting that they may be very difficult to differentiate during experiments using frequency data alone. In this case, a simple model such as the TBM can be used to simulate a wide range of conditions in order to study the crossing behavior of these modes. Overall, the TBM shows clear value for modeling this complex vibration problem when contact stiffness alone is considered. Next, damping in the contact is considered.

B. Damped contact vibrations

The second set of results is dedicated to tip-sample contact that includes damping effects. For this case, the TBM solution given by Eq. (14) must be solved for both the real and imaginary parts of the complex wavenumber. Because this solution is not as simple as the undamped case, a discussion of the solution space is first illustrated. Figure 6 is a plot of the value of the characteristic equation in terms of the real (horizontal axis) and imaginary (vertical axis) values of the complex wavenumber with darker colors indicating lower values. Thus, the solution for a given mode is found when this function reaches a local minimum. Results for the first six modes are indicated for a given set of contact conditions ($\alpha_n = 100$ and $\beta_n = 1$; other contact elements are zero). For the case without damping, all modes would be restricted to the horizontal axis because the imaginary part of all wavenumbers would be zero. As the damping increases, the modes obtain an imaginary part. As these results show, the magnitude of the imaginary part is not a simple function of β_n, but is a function of the modal response.[18] Thus, this result highlights the challenges of this damped vibration problem with respect to the root-finding algorithm. For example, the third and fourth modes (for this case with κ_{real} near 6.5) may have closely spaced root basins that can make it difficult to find all modes without very good initial guesses that are close to the minima. In addition, the trend with respect to the amount of damping is different for each mode. As illustrated for the values chosen, for each pair of modes (one symmetric, one asymmetric), the symmetric is more sensitive to the damping than the asymmetric one primarily because of the mode shape. In the results that follow, the minima are tracked using small changes in contact parameters in order for the values of the complex wavenumbers to be identified.

The results from the damped vibrations are examined with respect to the quality factors for each mode. Using Eqs. (20) and (34), values of Q for the TBM and FEM can be calculated from the complex wavenumbers of each model. Results for two different cases of contact stiffness are shown in Tables I and II. In Table I, $\alpha_n = 100$ and the other two contact stiffnesses are 85% of that value. In Table II, all stiffness values are one tenth of those in Table I. In each case, the transverse and axial dimensionless damping parameters are also assumed to be 85% of the normal damping. As before, only the six lowest modes are examined. The results are tabulated according to β_n. For all cases, the damping is assumed to be much lower than the contact stiffness such that $\kappa_{imag} \ll \kappa_{real}$. Thus, the damping is allowed to vary up to 1% of the dimensionless contact stiffness.

The differences in Q-factor between the two models stay nearly constant for the different values of dimensionless contact damping, β_n. For the higher stiffness case, Table I, except for the second asymmetric mode, all quality factors from the TBM are underpredicted relative to the FEM. The first symmetric mode is about 9% lower than the FEM, and for the first asymmetric the TBM solution is about 2% lower than the FEM. The second symmetric mode has an error of less than 7%, and for the higher mode the error is greater. The maximum error for both cases occurs for the highest

TABLE I. Comparison of the quality factor Q for values of β_n for both the analytical TBM and numerical FEM for the case with $\alpha_n = 100$, $\alpha_a = \alpha_t = 0.85\alpha_n$, and $\beta_a = \beta_t = 0.85\beta_n$.

	$\beta_n = 0.001$			$\beta_n = 0.01$			$\beta_n = 0.1$			$\beta_n = 1$		
	Q_{FEM}	Q_{TBM}	Dif.%	Q_{FEM}	Q_{TBM}	Dif.%	Q_{FEM}	Q_{TBM}	Dif.%	Q_{FEM}	Q_{TBM}	Dif.%
1st Flexural Sym.	6.27×10^4	5.71×10^4	−8.94	6.27×10^3	5.71×10^3	−8.94	6.27×10^2	5.71×10^2	−8.93	6.35×10^1	5.81×10^1	−8.54
1st Flexural Asym.	4.76×10^5	4.67×10^5	−1.98	4.76×10^4	4.67×10^4	−1.98	4.76×10^3	4.67×10^3	−1.98	4.76×10^2	4.67×10^2	−1.96
2nd Flexural Sym.	6.15×10^3	5.74×10^3	−6.61	6.15×10^2	5.74×10^2	−6.61	6.15×10^1	5.74×10^1	−6.59	6.25×10^0	5.90×10^0	−5.57
2nd Flexural Asym.	6.23×10^4	6.99×10^4	12.3	6.23×10^3	6.99×10^3	12.3	6.23×10^2	6.99×10^2	12.3	6.23×10^1	6.99×10^1	12.3
3rd Flexural Sym.	4.49×10^3	4.02×10^3	−10.5	4.49×10^2	4.02×10^2	−10.5	4.49×10^1	4.02×10^1	−10.6	4.28×10^0	3.74×10^0	−12.7
3rd Flexural Asym.	6.45×10^4	5.63×10^4	−12.7	6.45×10^3	5.63×10^3	−12.7	6.45×10^2	5.63×10^2	−12.7	6.44×10^1	5.63×10^1	−12.6

TABLE II. Comparison of the quality factor Q for values of β_n for both the analytical TBM and numerical FEM for the case with $\alpha_n = 10$, $\alpha_a = \alpha_t = 0.85\alpha_n$, and $\beta_a = \beta_t = 0.85\beta_n$.

	$\beta_n = 0.0001$			$\beta_n = 0.001$			$\beta_n = 0.01$			$\beta_n = 0.1$		
	Q_{FEM}	Q_{TBM}	Dif.%	Q_{FEM}	Q_{TBM}	Dif.%	Q_{FEM}	Q_{TBM}	Dif.%	Q_{FEM}	Q_{TBM}	Dif.%
1st Flexural Sym.	1.65×10^4	1.58×10^4	−4.37	1.65×10^3	1.58×10^3	−4.37	1.65×10^2	1.58×10^2	−4.37	1.65×10^1	1.58×10^1	−4.43
1st Flexural Asym.	4.08×10^6	4.05×10^6	−0.74	4.08×10^5	4.05×10^5	−0.73	4.08×10^4	4.05×10^4	−0.73	4.08×10^3	4.05×10^3	−0.73
2nd Flexural Sym.	1.75×10^4	1.69×10^4	−3.20	1.75×10^3	1.69×10^3	−3.20	1.75×10^2	1.69×10^2	−3.20	1.74×10^1	1.69×10^1	−2.79
2nd Flexural Asym.	5.66×10^5	6.37×10^5	12.6	5.66×10^4	6.37×10^4	12.6	5.66×10^3	6.37×10^3	12.6	5.66×10^2	6.37×10^2	12.6
3rd Flexural Sym.	5.70×10^4	5.34×10^4	−6.40	5.70×10^3	5.34×10^3	−6.40	5.70×10^2	5.34×10^2	−6.40	5.70×10^1	5.34×10^1	−6.37
3rd Flexural Asym.	6.41×10^5	5.57×10^5	−13.1	6.41×10^4	5.57×10^4	−13.1	6.41×10^3	5.57×10^3	−13.1	6.41×10^2	5.57×10^2	−13.1

evaluated mode, the third asymmetric mode, and is about 13%. Although these results show clear differences between the TBM and the FEM, the TBM estimates are very stable with respect to changes in tip-sample contact properties. Thus, it seems that future improvements to the model may allow such differences to be reduced.

V. CONCLUSIONS

In this article, the contact vibration response of a U-shaped thermal AFM probe has been examined using a simplified analytical model (TBM) and the more complex FEM. For both cases, the contact was modeled using three orthogonal spring-dashpot elements in order for the resonant frequencies and Q-factors to be determined. The results for contact stiffness alone showed that the TBM approximation is very good when compared with FEM over a wide range of contact stiffness values. Results for in-plane or out-of-plane stiffness alone as well as in combination suggest that the TBM can predict resonant frequencies to within 8% of the FEM for the first six modes. In addition, a viscoelastic contact was modeled in order for the resonant frequencies and Q-factors to be determined for each mode. In this case, the results show that TBM is a good approximation with respect to FEM for contact conditions involving both stiffness and damping in the contact.

The mapping of viscoelastic properties experimentally, even for a small area of interest, may require several hundred measurements of contact resonance spectra. Each measurement must be analyzed if the sample properties are to be determined quantitatively. Assuming a reasonable number of elements, the FEM will be much slower (several hundred times) than the TBM highlighting the utility of such an approximate approach. In addition, the variability of probe manufacturing makes it very difficult to generate FEM meshes that are well-suited for a given probe. Thus, we expect that approximate analytical models such as the TBM will prove themselves useful for *in-situ* analysis during AFM imaging. In addition, simple models will allow a wide range of measurement parameters to be simulated quickly in order for predictions to be made for a given sample. Because CR-AFM spectra can be difficult to interpret for U-shaped probes,[24] simple models may allow these spectra to be understood with greater clarity. Finally, the differences in the TBM predictions from the FEM may not be very important, especially if relative measurements (i.e., using a reference sample) are possible. The prospects for quantitative thermomechanical experiments on polymers are very exciting.

APPENDIX: CONTINUITY CONDITIONS FOR THE CONTACT CASE

The contact between the tip and the sample is assumed to be the source of all loads that may result for the contact vibration problem. For the analytical model, the contact is assumed to act at a single point. The displacement and velocity of this point create the relevant loads between the probe and the sample. These loads are in the three orthogonal directions corresponding with the spring-dashpot elements assumed. At the same time, all the continuity conditions between the two legs and the probe crossbeam need to be defined with the tip-sample contact in mind. Consequently, these loads must be transferred from the contact point of the tip to the joints. This transfer causes the contact forces to appear within the continuity conditions in the form of the forces and moments that are generated. This concept is illustrated schematically in Fig. 7. For simplicity, the axial load, the transverse load, and the moment about the z-axis are neglected. Thus, the other forces and moments are given by

$$F_n = -k_n \times w_3(0,t) - c_n \times \dot{w}_3(0,t), \tag{A1}$$

$$M_t = F_t \times H_z = -k_t \times w_3'(0,t) \times H_z^2 - c_t \times \dot{w}_3'(0,t) \times H_z^2, \tag{A2}$$

$$M_a = F_a \times H_z + F_n \times H_x = -k_a \times H_z^2 \times \phi_3(0,t) - c_a \times H_z^2 \times \dot{\phi}_3(0,t) - k_n \times w_3(0,t) \times H_x - c_n \times \dot{w}_3(0,t) \times H_x. \tag{A3}$$

Similar to the contact loads, there are some loads due to the mass moment of inertia of the beams, as illustrated in Fig. 8. They are defined at the mid-point of the cross beam, but once again they need to be transferred to the joint in order to be included in the continuity conditions for the eigenvalue

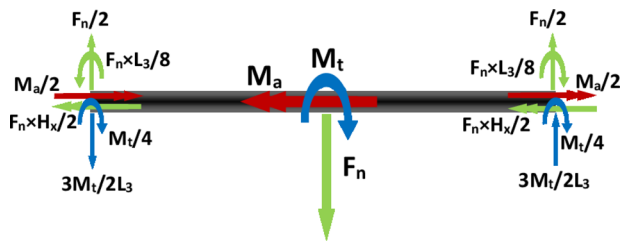

FIG. 7. Free body diagram of the cross beam considering the external forces from the springs and dashpots assumed present in the tip-sample contact.

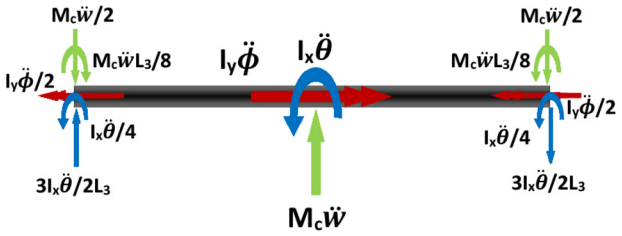

FIG. 8. Moment of inertia of the cross beam.

problem. Substitution of the contact and mass moment of inertia loads into the continuity conditions, the six continuity conditions for forces and moments at the joint can be stated as

$$\tilde{w}_1'''(1,\tau) - \frac{(EI)_3}{(EI)_1\tilde{L_3}^2}\tilde{w}_3'''\left(-\frac{1}{2},\tau\right) + \tilde{C}_1 - \tilde{C}_4 - \widetilde{MM}_1 + \widetilde{MM}_3 = 0, \tag{A4}$$

$$\tilde{\phi}_1'(1,\tau) - \frac{(EI)_3}{(GK)_1\tilde{L_3}}\tilde{w}_3''\left(-\frac{1}{2},\tau\right) + \tilde{C}_2 - \tilde{C}_5 - \widetilde{MM}_2 + \widetilde{MM}_4 = 0, \tag{A5}$$

$$\tilde{w}_1''(1,\tau) - \frac{(GK)_3}{(EI)_1\tilde{L_3}}\tilde{\phi}_3'\left(-\frac{1}{2},\tau\right) + \tilde{C}_6 + \tilde{C}_3 - \widetilde{MM}_5 = 0, \tag{A6}$$

$$\tilde{w}_2'''(1,\tau) + \frac{(EI)_3}{(EI)_1\tilde{L_3}^2}\tilde{w}_3'''\left(\frac{1}{2},\tau\right) + \tilde{C}_1 + \tilde{C}_4 - \widetilde{MM}_1 - \widetilde{MM}_3 = 0, \tag{A7}$$

$$\tilde{\phi}_2'(1,\tau) + \frac{(EI)_3}{(GK)_1\tilde{L_3}}\tilde{w}_3''\left(\frac{1}{2},\tau\right) - \tilde{C}_2 - \tilde{C}_5 + \widetilde{MM}_2 + \widetilde{MM}_4 = 0, \tag{A8}$$

$$\tilde{w}_2''(1,\tau) + \frac{(GK)_3}{(EI)_1\tilde{L_3}}\tilde{\phi}_3'\left(\frac{1}{2},\tau\right) + \tilde{C}_6 + \tilde{C}_3 - \widetilde{MM}_5 = 0, \tag{A9}$$

where the dimensionless variables $\tilde{C}_i$ are related to the contact forces, and the dimensionless variables $\widetilde{MM}_i$ are from mass moments of inertia. The following equations state these expressions in a more convenient form for use in the continuity conditions:

$$\tilde{C}_1 = \frac{L^2}{(EI)_1}\frac{F_n}{2} = -\frac{L^3}{6EI}k_n\,3\tilde{L_3}\tilde{w}_3(0,\tau) - i\,c_n\sqrt{\frac{L^2}{36EI\,\rho A}}3\kappa^2\tilde{L_3}\tilde{w}_3(0,\tau),$$

$$\tilde{C}_2 = \frac{L}{(GK)_1}\frac{F_nL_3}{8} = -\frac{L^3}{6EI}k_n\frac{3\tilde{L_3}}{4R}\tilde{L_3}\tilde{w}_3(0,\tau) - i\,c_n\sqrt{\frac{L^2}{36EI\,\rho A}}\frac{3\tilde{L_3}}{4R}\kappa^2\tilde{L_3}\tilde{w}_3(0,\tau),$$

$$\tilde{C}_3 = \frac{L}{(EI)_1}\frac{F_n\times H_x}{2} = -\frac{L^3}{6EI}k_n\,3\tilde{H}_x\tilde{L_3}\tilde{w}_3(0,\tau)) - i\,c_n\sqrt{\frac{L^2}{36EI\,\rho A}}3\kappa^2\,\tilde{H}_x\tilde{L_3}\tilde{w}_3(0,\tau),$$

$$\tilde{C}_4 = \frac{L^2}{(EI)_1}\frac{3}{2}\frac{F_t\times H_z}{L_3} = -\frac{L^3}{6EI}k_t\frac{9}{\tilde{L_3}}\tilde{w}_3'(0,\tau)\tilde{H}_z^2 - i\,c_t\sqrt{\frac{L^2}{36EI\,\rho A}}\frac{9}{\tilde{L_3}}\kappa^2\,\tilde{w}_3'(0,\tau)\tilde{H}_z^2,$$

$$\tilde{C}_5 = \frac{L}{(GK)_1}\frac{F_t\times H_z}{4} = -\frac{L^3}{6EI}k_t\frac{3}{2R}\tilde{w}_3'(0,\tau)\tilde{H}_z^2 - i\,c_t\sqrt{\frac{L^2}{36EI\,\rho A}}\frac{3}{2R}\kappa^2\,\tilde{w}_3'(0,\tau)\tilde{H}_z^2,$$

$$\tilde{C}_6 = \frac{L}{(EI)_1}\frac{F_a\times H_z}{2} = -\frac{L^3}{6EI}k_a\,3\tilde{H}_z^2\tilde{\phi}_3(0,\tau) - i\,c_a\sqrt{\frac{L^2}{36EI\,\rho A}}3\kappa^2\,\tilde{H}_z^2\tilde{\phi}_3(0,\tau).$$

The forces and moments which correspond with the mass moments of inertia can be simplified as

$$\widetilde{MM}_1 = \frac{L^2}{(EI)_1}\frac{M_c\ddot{\tilde{w}}_3(0,\tau)L_3}{2} = -\frac{S_2S_5}{2S_3}\kappa^4\tilde{w}_3(0,\tau), \tag{A10}$$

$$\widetilde{MM}_2 = \frac{L}{(GK)_1}\frac{M_c\ddot{\tilde{w}}_3(0,\tau)L_3^2}{8} = -\frac{S_2^2S_5}{8R\,S_3}\kappa^4\tilde{w}_3(0,\tau), \tag{A11}$$

$$\widetilde{MM}_3 = \frac{L^2}{(EI)_1}\frac{\frac{3}{2}I_x\ddot{\tilde{w}}_3'(0,\tau)}{L_3} = -\frac{\tilde{b_3}\tilde{L_3}^2 + \tilde{b_3}\tilde{h}^2}{8\tilde{b_1}}\kappa^4\tilde{w}_3'(0,\tau) \approx -\frac{\tilde{b_3}\tilde{L_3}^2}{8\tilde{b_1}}\kappa^4\tilde{w}_3'(0,\tau) = -\frac{S_2S_5}{8S_3}\kappa^4\tilde{w}_3'(0,\tau), \tag{A12}$$

$$\widetilde{MM}_4 = \frac{L}{(GK)_1}\frac{I_x\ddot{\tilde{w}}_3'(0,\tau)}{4} = -\frac{\tilde{b_3}\tilde{L_3}^3 + \tilde{b_3}\tilde{L_3}\tilde{h}^2}{48R\tilde{b_1}}\kappa^4\tilde{w}_3'(0,\tau) \approx -\frac{\tilde{b_3}\tilde{L_3}^3}{48R\tilde{b_1}}\kappa^4\tilde{w}_3'(0,\tau) = -\frac{S_2^2S_5}{48RS_3}\kappa^4\tilde{w}_3'(0,\tau), \tag{A13}$$

$$\widetilde{MM}_5 = \frac{L}{(EI)_1}\frac{I_y\ddot{\tilde{\phi}}_3(0,\tau)}{2} = -\frac{\tilde{b_3}^3\tilde{L_3} + \tilde{b_3}\tilde{L_3}\tilde{h}^2}{24\tilde{b_1}}\kappa^4\tilde{\phi}_3(0,\tau) \approx -\frac{\tilde{b_3}^3\tilde{L_3}}{24\tilde{b_1}}\kappa^4\tilde{\phi}_3(0,\tau) = -\frac{S_5^3R}{2S_2^2S_3}\kappa^4\tilde{\phi}_3(0,\tau), \tag{A14}$$

where $R = \frac{GK}{EI}$. For the case in which the legs and cross beam have the same material properties and thickness with assumed rectangular cross-section, the dimensionless parameters S_i can be reduced to simple forms as

$$S_1 = 1,\ S_2 = \tilde{L_3},\ S_3 = \sqrt{\frac{\tilde{b_1}^2}{12R}},\ S_4 = S_3,\ S_5 = \sqrt{\frac{\tilde{L_3}^2 \tilde{b_3}^2}{12R}}. \tag{A15}$$

These quantities have a physical interpretation. S_1 and S_2 define the bending stiffness of beams 2 and 3, respectively, relative to that of beam 1. S_3, S_4, and S_5 define the torsional stiffness of beams 1, 2, and 3, respectively, relative to the bending stiffness of beam 1.

The two terms of mass moment of inertia are

$$I_x = \frac{M_c}{12}\left(\tilde{L_3}^2 + \tilde{h}^2\right) \quad I_y = \frac{M_c}{12}\left(\tilde{b_3}^2 + \tilde{h}^2\right). \tag{A16}$$

Use of the dimensionless contact damping and contact stiffness allows the above relation to be simplified as

$$\tilde{C}_1 = -3\alpha_n S_2 \tilde{w}_3(0,\tau)) - i\,3\beta_n \kappa^2 S_2 \tilde{w}_3(0,\tau), \tag{A17}$$

$$\tilde{C}_2 = -\frac{3S_2^2}{4R}\alpha_n \tilde{w}_3(0,\tau) - i\,\frac{3S_2^2}{4R}\beta_n \kappa^2 \tilde{w}_3(0,\tau), \tag{A18}$$

$$\tilde{C}_3 = -3\alpha_n \tilde{H}_x S_2 \tilde{w}_3(0,\tau)) - i\,3\beta_n \kappa^2 \tilde{H}_x S_2 \tilde{w}_3(0,\tau), \tag{A19}$$

$$\tilde{C}_4 = -\frac{9\tilde{H}_z^2}{S_2}\alpha_t \tilde{w}_3'(0,\tau) - i\,\frac{9\tilde{H}_z^2}{S_2}\beta_t \kappa^2\, \tilde{w}_3'(0,\tau), \tag{A20}$$

$$\tilde{C}_5 = -\frac{3\tilde{H}_z^2}{2R}\alpha_t \tilde{w}_3'(0,\tau) - i\,\frac{3\tilde{H}_z^2}{2R}\beta_t \kappa^2\, \tilde{w}_3'(0,\tau), \tag{A21}$$

$$\tilde{C}_6 = -3\tilde{H}_z^2 \alpha_a \tilde{\phi}_3(0,\tau) - i\,3\tilde{H}_z^2 \beta_a \kappa^2\, \tilde{\phi}_3(0,\tau), \tag{A22}$$

where dimensionless contact stiffness and contact damping for the three orthogonal directions are defined as

$$\alpha_{n,t,a} = \frac{k_{n,t,a}}{\frac{6EI}{L^3}} \qquad \beta_{n,t,a} = c_{n,t,a}\sqrt{\frac{L^2}{36EI\,\rho A}}. \tag{A23}$$

By separation of variables, the governing equations given by Eqs. (1) and (2) can be solved.[32] For the flexural and the torsional motions of the beams, we seek solutions of the form

$$\begin{aligned} \tilde{w}_i &= X_i(\tilde{x})\,T(\tau), \\ \tilde{\phi}_i &= \Phi_i(\tilde{x})\,T(\tau), \end{aligned} \tag{A24}$$

where X_i, Φ_i, and T are functions of a single independent variable only, $\tilde{x}$ for $\tilde{w}_1$, $\tilde{w}_2$, $\tilde{\phi}_1$, $\tilde{\phi}_2$ ($\tilde{y}$ for $\tilde{w}_3$, $\tilde{\phi}_3$) or τ, respectively.

The entire beam oscillates at the same frequency for a given mode, thus the time dependence for each equation is identical. However, the wavenumbers for the flexural and torsional motion are different for each beam. The boundary conditions at the clamped end of the legs allow the spatial dependence for flexure to be written as[32]

$$\begin{aligned} X_1(\tilde{x}) &= A_1(\sin(\kappa\tilde{x}) - \sinh(\kappa\tilde{x})) + B_1(\cos(\kappa\tilde{x}) - \cosh(\kappa\tilde{x})), \\ X_2(\tilde{x}) &= A_2(\sin(S_1\,\kappa\tilde{x}) - \sinh(S_1\,\kappa\tilde{x})) + B_2(\cos(S_1\,\kappa\tilde{x}) - \cosh(S_1\,\kappa\tilde{x})), \\ X_3(\tilde{y}) &= A_3\,\sin(S_2\,\kappa\tilde{y}) + B_3\,\cos(S_2\,\kappa\tilde{y}) + C_3\sinh(S_2\,\kappa\tilde{y}) + D_3\cosh(S_2\,\kappa\tilde{y}), \end{aligned} \tag{A25}$$

and the spatial dependence for the torsional motion to be written as

$$\begin{aligned} \Phi_1(\tilde{x}) &= E_1\,\sin(S_3\,\kappa^2\tilde{x}), \\ \Phi_2(\tilde{x}) &= E_2\,\sin(S_4\,\kappa^2\tilde{x}), \\ \Phi_3(\tilde{y}) &= E_3\,\sin(S_5\,\kappa^2\tilde{y}) + F_3\,\cos(S_5\,\kappa^2\tilde{y}). \end{aligned} \tag{A26}$$

The continuity conditions for the contact case can be obtained by substituting the derivatives of Eqs. (A25) and (A26), Eqs. (A10)–(A14), and Eqs. (A17)–(A22) into Eqs. (A4)–(A9). The result is a system of 12 equations for the 12 coefficients, A_i, B_i, C_i, D_i, E_i, F_i, and wavenumber κ, but the full set of equations is not given here for brevity.

[1]U. Rabe, J. Turner, and W. Arnold, Appl. Phys. A **66**, S277 (1998).
[2]K. Yamanaka and S. Nakano, Appl. Phys. A **66**, S313 (1998).
[3]U. Rabe, S. Amelio, E. Kester, V. Scherer, S. Hirsekorn, and W. Arnold, Ultrasonics **38**, 430 (2000).
[4]D. C. Hurley, M. Kopycinska-Muller, E. D. Langlois, A. B. Kos, and N. Barbosa, Appl. Phys. Lett. **89**, 021911 (2006).
[5]S. Amelio, A. Goldade, U. Rabe, V. Scherer, B. Bhushan, and W. Arnold, Thin Solid Films **392**, 75 (2001).
[6]D. C. Hurley, K. Shen, N. M. Jennett, and J. A. Turner, J. Appl. Phys. **94**, 2347 (2003).
[7]D. C. Hurley and J. A. Turner, J. Appl. Phys. **102**, 033509 (2007).
[8]G. Stan, S. Krylyuk, A. Davydov, M. Vaudin, L. Bendersky, and R. Cook, Ultramicroscopy **109**, 929 (2009).
[9]G. Stan and R. F. Cook, Nanotechnology **19**, 235701 (2008).
[10]P. A. Yuya, D. C. Hurley, and J. A. Turner, J. Appl. Phys. **104**, 074916 (2008).
[11]J. P. Killgore, D. G. Yablon, A. H. Tsou, A. Gannepalli, P. A. Yuya, J. A. Turner, R. Proksch, and D. C. Hurley, Langmuir **27**, 13983 (2011).
[12]D. C. Hurley, S. E. Campbell, J. P. Killgore, L. M. Cox, and Y. Ding, Macromolecules **46**, 9396 (2013).
[13]D. G. Yablon, J. Grabowski, and I. Chakraborty, Meas. Sci. Technol. **25**, 055402 (2014).
[14]D. G. Yablon, A. Gannepalli, R. Proksch, J. Killgore, D. C. Hurley, J. Grabowski, and A. H. Tsou, Macromolecules **45**, 4363 (2012).
[15]R. C. Tung, J. P. Killgore, and D. C. Hurley, Rev. Sci. Instrum. **84**, 073703 (2013).
[16]A. Gannepalli, D. G. Yablon, A. H. Tsou, and R. Proksch, Nanotechnology **22**, 355705 (2011).
[17]U. Rabe, K. Janser, and W. Arnold, Rev. Sci. Instrum. **67**, 3281 (1996).
[18]P. A. Yuya, D. C. Hurley, and J. A. Turner, J. Appl. Phys. **109**, 113528 (2011).
[19]R. Wagner, J. P. Killgore, R. C. Tung, A. Raman, and D. C. Hurley, Nanotechnology **26**, 045701 (2015).
[20]J. A. Turner and J. S. Wiehn, Nanotechnology **12**, 322 (2001).
[21]B. Lee and W. P. King, Rev. Sci. Instrum. **83**, 074902 (2012).

[22]S. Somnath, J. O. Liu, M. Bakir, C. B. Prater, and W. P. King, Nanotechnology **25**, 395501 (2014).
[23]E. Dillon, K. Kjoller, and C. Prater, Microsc. Today **21**, 18 (2013).
[24]J. P. Killgore, R. C. Tung, and D. C. Hurley, Nanotechnology **25**, 345701 (2014).
[25]B. J. Rodriguez, C. Callahan, S. V. Kalinin, and R. Proksch, Nanotechnology **18**, 475504 (2007).
[26]S. E. Campbell, V. L. Ferguson, and D. C. Hurley, Acta Biomater. **8**, 4389 (2012).
[27]K. Yamanaka, Y. Maruyama, T. Tsuji, and K. Nakamoto, Appl. Phys. Lett. **78**, 1939 (2001).
[28]D. C. Hurley and J. A. Turner, J. Appl. Phys. **95**, 2403 (2004).
[29]H. Wagner, D. Bedorf, S. Küchemann, M. Schwabe, B. Zhang, W. Arnold, and K. Samwer, Nat. Mater. **10**, 439 (2011).
[30]K. Park, A. Marchenkov, Z. M. Zhang, and W. P. King, J. Appl. Phys. **101**, 094504 (2007).
[31]W. P. King, B. Bhatia, J. R. Felts, H. J. Kim, B. Kwon, B. Lee, S. Somnath, and M. Rosenberger, Annu. Rev. Heat Transfer **16**, 287 (2013).
[32]E. Rezaei and J. A. Turner, J. Appl. Phys. **115**, 174302 (2014).
[33]Anasys Instruments, Santa Barbara, California.
[34]L. Meirovitch, *Fundamentals of Vibrations* (McGraw-Hill College, New York City, U.S., 2000).
[35]S. S. Rao, *Vibration of Continuous Systems* (John Wiley & Sons, 2007).